Structural Reorganization of Proteins Revealed by Radiolysis and Mass Spectrometry: G-Actin Solution Structure Is Divalent Cation Dependent†

Jing-Qu Guan,‡,§ Steven C. Almo,‡,|| Emil Reisler,⊥ and Mark R. Chance*,‡,§,||

Center for Synchrotron Biosciences, Department of Physiology and Biophysics, and Department of Biochemistry, Albert Einstein College of Medicine, 1300 Morris Park Avenue, Bronx, New York 10461, and Department of Chemistry and Biochemistry and Molecular Biology Institute, University of California, Los Angeles, California 90095

Received May 29, 2003; Revised Manuscript Received August 4, 2003

ABSTRACT: The solution structures of isolated monomeric actins in their Mg^{2+}-ATP and Ca^{2+}-ATP bound forms and in complexes with gelsolin segment-1 have been probed using hydroxyl radicals (·OH) generated by synchrotron X-ray radiolysis. Proteolysis and mass spectrometry analysis of 28 peptides containing 58 distinct reactive probe sites within actin were used to monitor conformational variations linked to divalent cation and gelsolin segment-1 binding. The solvent accessibilities of the probe sites, as measured by footprinting in solution for the Ca^{2+}-G-actin and Mg^{2+}-G-actin complexes with gelsolin segment-1, were consistent with available crystallographic data. This included a specific protection at the contact interface between the partners, as revealed by reduced reactivity of peptide 337−359 in the complex. Aside from the specific protection indicated previously, the oxidation rates for the reactive residues of the isolated Ca^{2+}-G-actin were similar to those of the actin gelsolin segment-1 complexes; however, the reactivity of numerous residues in the isolated Mg^{2+}-G-actin form was significantly reduced. Specifically, Mg^{2+}-G-actin has a set of protected sites relative to Ca^{2+}-G-actin that suggest a structural reorganization in subdomains 4 and 2 and a C-terminus more closely packed onto subdomain 1. These conformational variations for isolated Mg^{2+}-G-actin provide a structural basis for its greater tendency to polymerize into filaments as compared to Ca^{2+}-G-actin.

In eukaryotic cells, actin undergoes monomer−polymer transitions that mediate cell shape and control essential processes including locomotion, vescicle transport, and cytokinesis (*1*−*2*). The polymerization of actin is a spontaneous process that is highly dependent upon both nucleotide and divalent cations (*3*−*11*). The tendency of G-actin[1] to polymerize has made the determination of the three-dimensional structure of isolated actin monomers by X-ray crystallography or NMR relatively difficult. Nonetheless, a number of high-resolution crystal structures of actin complexes are available (*12*−*17*) since the ability of G-actin to polymerize is impaired upon formation of complexes with actin-binding proteins such as profilin, gelsolin segment-1 (GS1), bovine pancreatic deoxyribonuclease I (DNase I), or vitamin D-binding proteins. The covalent binding of a fluorophore (tetramethyl rhodamine-5-maleimide) to Cys-374 also blocks polymerization, and a high-resolution structure of this form of ADP-actin is available (*18*). On the basis of these crystallographic data, it has been suggested that the conformation of subdomain 2 is particularly flexible and linked to filament assembly (*4*, *5*, *8*, *9*, *19*−*21*).

Radiolytic protein footprinting provides a quantitative approach to monitor changes in surface accessibility of specific amino acid side chains (*22*−*28*). Hydroxyl radicals generated from millisecond exposure of aqueous solutions to synchrotron radiation react with proteins and result in stable oxidative modifications of solvent accessible amino acid side chains. The extents and sites of oxidative modification can be quantified using proteolytic digestion and mass spectrometry. The most reactive residues, which represent the most easily observed experimental probes for this method, include surface accessible cysteine, methionine, phenylalanine, tyrosine, tryptophan, histidine, proline, and leucine side chains (*24*, *29*). In this paper, we explore the structures of isolated ATP-bound actin monomers and complexes in solution using synchrotron protein footprinting. The results show divalent cation-dependent conformational variations of the isolated actin monomers and suggest a structural basis for the greater tendency of Mg^{2+}-ATP actin monomers to polymerize.

† This work is supported through the Innovative Molecular Analysis Technologies Program of the National Cancer Institute (R33-CA-84173), the Technology Centers Program of the National Institute for Biological Imaging and Bioengineering (P41-EB-01979), and Grants R01-GM-53807 and R01-AR-22031 from NIH and MCB-9904599 from NSF. The National Synchrotron Light Source at Brookhaven National Laboratory is supported by the Department of Energy, Division of Materials Sciences.

* To whom correspondence should be addressed. Phone: (718) 430-4136. Fax: (718) 430-8587. E-mail: mrc@aecom.yu.edu.

‡ Center for Synchrotron Biosciences, Albert Einstein College of Medicine.

§ Department of Physiology and Biophysics, Albert Einstein College of Medicine.

|| Department of Biochemistry, Albert Einstein College of Medicine.

⊥ University of California.

[1] Abbreviations: G-actin, monomeric actin; F-actin, filamentous actin; GS1, gelsolin segment-1; DTT, dithiothreitol; TFA, trifluoroacetic acid; HPLC, high performance liquid chromatography; MS, mass spectrometry; ESI, electronspray ionization; TIC, total ion chromatogram; DLS, dynamic light scattering.

10.1021/bi034914k CCC: $25.00
Published on Web 09/23/2003

EXPERIMENTAL PROCEDURES

Protein Purification. Rabbit skeletal muscle actin (Ca-G-actin) was prepared as described (*30*) and stored at 4 °C in Ca-G-buffer (2 mM Tris, pH 7.6, 0.2 mM ATP, 0.5 mM DTT, 0.2 mM $CaCl_2$, and 1mM NaN_3), which was freshly prepared and exchanged daily. Mg-F-actin was prepared by adding $MgCl_2$ and EGTA (final concentrations: $MgCl_2$, 2 mM and EGTA, 1 mM) to a solution of Ca-G-actin (25 μM) in Ca-G-buffer followed by incubation at 4 °C for 30 min. To ascertain the concentration at which Mg-actin is monomeric by using dynamics light scattering (see later), samples of actin at different concentrations were prepared and dialyzed against G-Mg-buffer (2 mM Tris, pH 7.6, 0.2 mM ATP, 0.5 mM DTT, 0.05 mM $MgCl_2$, and 1mM NaN_3) for 3 days before use, with daily changes of freshly prepared G-Mg-buffer. Under these conditions, the actin was demonstrated to be entirely monomeric, within the limit of detection. The complexes Ca-G-actin/GS1 and Mg-G-actin/GS1 were prepared as described previously (*23*).

Radiolysis. Prior to radiolysis experiments, Ca-G-actin and Mg-G-actin (5.0 μM) were dialyzed overnight against Ca-G-actin radiolysis buffer (2 mM sodium cacodylate pH 7.6, 0.05 mM $CaCl_2$, and 0.2 mM ATP) and Mg-G-actin radiolysis buffer (2 mM sodium cacodylate pH 7.6, 0.05 mM $MgCl_2$, and 0.2 mM ATP), respectively. All synchrotron exposure experiments were performed at the X-28C beamline of the National Synchrotron Light Source, Brookhaven National Laboratory. Exposure times were controlled by using an electronic shutter (Vincent Associates) and ranged from 0 to 200 ms. The storage ring energy was 2.8 GeV, and ring currents ranged from 136 to 289 mA throughout all the experiments in this study (*24*).

Enzymatic Proteolysis and MS Analysis. Radiolyzed samples were denatured in acetonitrile prior to proteolysis with sequencing grade modified trypsin, endoproteinase Asp-N, and endoproteinase Glu-C (Roche). Following enzymatic proteolysis, the resulting peptide mixtures were separated and analyzed using a coupled HPLC-ESI-MS LCQ system (ThermoFinnigan). Reverse phase HPLC was performed on a Waters 2690 Separations Module (Waters Corporation), using a C18 (Vydac) 1.0 × 150 mm column for all digested protein samples. Buffer A (95% water, 5% acetonitrile, and 0.06% TFA) and buffer B (90% acetonitrile, 10% water, and 0.055% TFA) were used to establish a gradient. The HPLC elute was directed to a Finigan LCQ quadrupole ion trap mass spectrometer with a needle voltage of 4.5 kV. The samples were scanned for 60−75 min, and the spectra were acquired in the positive ion mode for masses corresponding to an *m*/*z* range of 400−2000. The sites of oxidative modification were determined by tandem HPLC-MS/MS. For the acquisition of MS/MS data, a 1.0 unit *m*/*z* range was used in selecting the parent ion for fragmentation in the second stage of the mass spectrometer.

We report reactivity and MS/MS data for 28 separate peptides in this paper. Some peptides, like 311−362 (from the Asp-N digestion), are not reported since they included too many residues to provide a site-specific probe. Other peptides, such as 148−177 (from the tryptic digestion) and 3−10 and 211−221 (from the AspN digestion), did not ionize well enough in the ESI-MS to provide good signals for quantifying the oxidation extent. Thus, we report data only for those peptides that exhibited oxidation and whose oxidation rates were accurately measured for all four actin states analyzed in this paper.

Acetylated N-Terminus and Methylated His-73 Residues. The masses of the actin peptides were predicted using the program PAWS (Proteometrics, NY). However, rabbit skeletal muscle actin has known posttranslational modifications, including acetylation and methylation (*12*, *31*−*33*). A doubly charged ion peak for peptide 1−18 was detected at *m*/*z* 954.4 ($(M + CH_3CO + 2H)^{2+}$) as opposed to *m*/*z* 933.4 ($(M + 2H)^{2+}$), consistent to acetylation at the N-terminus. MS/MS provided direct evidence for the acetylation. Daughter ions of *y*-type are generated when the charge is retained on the C-terminus, the $y - 5$, $y - 7$, $y - 9$, $y - 10$, $y - 11$, $y - 12$, $y - 13$, and $y - 14$ ions are clearly seen as unshifted in Supporting Information Figure 1a. *B*-type ions are generated when a charge is retained on the N-terminus; all the observed *b*-ions (e.g., $b - 5$, $b - 6$, $b - 7$, $b - 8$, $b - 9$, $b - 10$, $b - 13$, $b - 14$, $b - 16$, and $b - 17$) are observed as shifted by +42 mass from the presence of the acetyl group on the N-terminus.

Likewise, both MS and MS/MS data suggest that residue His-73 is methylated in the rabbit skeletal muscle actin used in this study. A doubly charged ion at *m*/*z* 987.9 ($(M + CH_3 + 2H)^{2+}$) was monitored for peptide 69−84. Conversely, extraction within the total ion chromatogram for an ion corresponding to unmethylated peptide 69−84 provided no signal. MS/MS sequencing (Supporting Information Figure 1b) showed unshifted *y*-type ions for $y - 4$, $y - 6$, $y - 7$, $y - 8$, $y - 9$, and $y - 11$. However, the $y - 12$ ion was observed to have an *m*/*z* 1472.5 instead of 1458.6, consistent with methylation at His-73. Ions $y - 13$ (1601.3) and $y - 14$ (1715.9) also exhibited a mass increase of +14 units. The *y*-ion series is consistent with methylation at His-73 and is corroborated by the *b*-ion series derived from the N-terminus. While the smaller *b*-ions (i.e., $b - 1$ to $b - 4$) were undetected, all the detected *b*-ions ($b - 5$, $b - 6$, $b - 7$, $b - 8$, $b - 9$, $b - 10$, $b - 11$, $b - 12$, $b - 13$, and $b - 15$) were observed to have a mass increase of 14 units.

Dynamic Light Scattering (DLS). All DLS measurements were acquired by using a DynaPro MS/X Dynamic Light Scattering instrument (Protein Solutions, Charlottesville, VA) at 4 °C. Prior to the DLS experiments, NaN_3 and DTT in all samples were removed by dialysis against the appropriate G-buffer lacking NaN_3 and DTT. The three independent data were collected by the DynoPro Instrument Control Software Version 5.26. Control experiments showed no difference for samples in their original buffers (i.e., Ca-G-buffer and Mg-G-buffer) as compared to samples in radiolysis buffers. The time-dependent autocorrelation function of the photocurrent was acquired every 10 s, with 10 acquisitions for each run. The samples of Ca-G-actin at different concentrations were filtered through 0.2-μm filters (Millipore, Bedford, MA) before being used for the Mg-actin preparations. The sample protein solution in a Uvette cuvette (160−1600 nm cutoff, Eppendorf) was illuminated by an 824.6 nm laser, and the intensity of light scattered at an angle of 90° was measured by a solid-state avalanche photodiode.

Calculation of Surface Areas of Solvent Accessibilities. To verify the correlation of side-chain reactivity and solvent accessibility for selected side-chain residues in actin, the crystal structures of the complexes of Ca^{2+}-G-actin/DNase

Table 1: Calculation of Solvent Accessible Areas of Reactive Residues of Actin in the Ca-G-Actin/GS1 Complex, the Mg-G-Actin/GS1 Complex, and of Isolated Actin Obtained from the Actin/DNase I Complex with DNase I Removed[a]

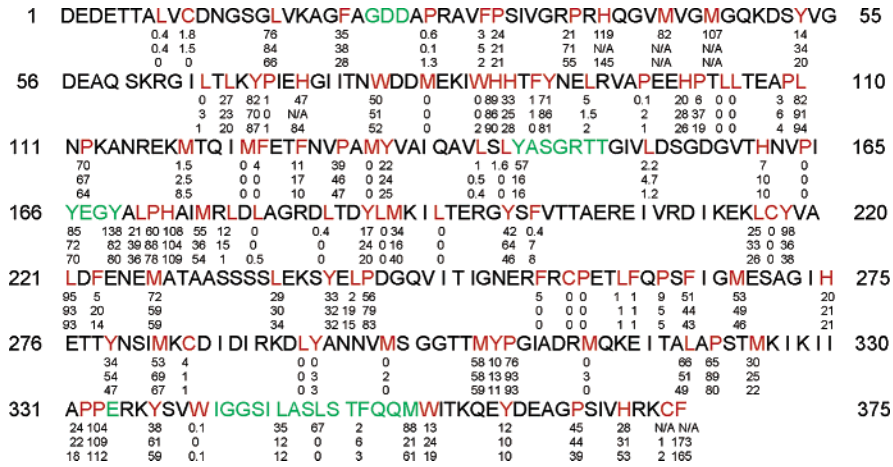

[a] The most reactive residues are colored in red, and the solvent accessible areas (Å^2) are given for actin (minus DNase I) (1st row), Ca-G-actin/GS1 (2nd row), and Mg-G-actin/GS1 (3rd row). The contact sites of actin with GS1 in the complexes are colored in green.

I (PDB 1ATN), Ca^{2+}-G-actin/GS1 (PDB 1EQY), and Mg^{2+}-G-actin/GS1 (PDB 1D4X) were analyzed using the program VADAR 1.2 (the Canadian Protein Engineering Network, University of Alberta, Canada), as described previously (*23*, *24*).

Modification Rates. Dose responses data were obtained from the LCQ spectra of the digested peptide samples. The integrated areas of the modified and unmodified peptide ions in the total ion chromatogram were used to calculate the modification extent (the ratio of integrated area of the unmodified peptide to the sum of integrated areas from the modified and unmodified peptides). Throughout all the calculations, the most abundant charge state (usually doubly charged) was used; the calculation of the modified total included all observed products (e.g., +16, +32, etc.), and any background modification seen in the unexposed sample was subtracted from the totals. The dose response curves are presented as an unmodified fraction (plotted on a logarithmic scale) versus X-ray exposure time and are fitted to the equation $A = A_0e^{-kt}$, in which A and A_0 are the amount of a peptide at time t and 0, respectively, and k is the modification rate constant (Origin 5.0, Microcal Software, Inc.). All data presented are an average of three independent experiments; the errors are the standard deviations of these measurements (Excel 2000, Microsoft).

RESULTS

Proteolysis of Actin and Solvent Accessible Surfaces Predicted from Crystallographic Data. Three proteases, trypsin, Asp-N, and Glu-C, have been used in this study to generate as many peptides as possible to probe actin structure. In addition, we have redundant information on the reactivity for some peptides where modifiable residues overlap. The 28 peptides examined cover ~90% of the actin sequence, including the DNase-I binding loop (D-loop) (monitored as residues 40−50 from the trypsin digestion), the N-terminus (residues 1−18, trypsin digestion), the C-terminus (residues 360−372, trypsin digestion and residues 363−375, Asp-N digestion), and the putative hydrophobic loop (H-loop) (residues 260−270 from the Glu-C digestion) proposed by Holmes et al. (*34*) to be important to F-actin structure.

The solvent accessible surface areas of the most reactive side chains are shown in Table 1 for three crystallographic structures, including Mg^{2+} and Ca^{2+} bound actin/gelsolin segment-1 complexes and a Ca^{2+}-G-actin/DNase I structure. DNase I was removed from the PDB file prior to the VADAR calculation in the case of the Ca^{2+}-G-actin/DNase I structure, so that the accessibility of the loop in subdomain 2 (residues 38−52) could be properly evaluated for the actin monomer. The residues predicted to be most reactive on the basis of known chemistry and solvent accessibility are colored in red in Table 1. Solvent accessible surface areas for the side chains (shown in Å^2) of actin/(minus DNase I), first row; Ca^{2+}-G-actin/GS1, second row; and Mg^{2+}-G-actin/GS1, third row are indicated underneath these residues. The solvent accessible area values for these three actin forms are very similar, except for those residues that lie in the contact interface of G-actin with GS1 (colored in green in Table 1). For example, Leu 349 has a solvent accessible area value of 67 Å^2 for the Ca^{2+}-G-actin/DNase I structure, while this value drops to 0 for both GS1 complexes. Similarly, Met-355 has a solvent accessible area value of 88 Å^2 for the Ca^{2+}-G-actin/DNase I structure; these values drop to 21 and 61 Å^2 for the Ca^{2+} and Mg^{2+}-G-actin-GS1 complexes, respectively. Solvent accessible area values for the residues in the loop 39−52 of actin are not available for the Ca^{2+}-G-actin-GS1 or Mg^{2+}-G-actin-GS1 complexes since they are disordered in the electron density maps. This loop is quite solvent accessible based on a calculation of its structure from the G-actin/DNase I complex with DNase I removed.

Correlation of Side-Chain Reactivity with Surface Accessibility in Actin and Its Complexes. The complexes Ca-G-actin/GS1 and Mg-G-actin/GS1 and the Ca- and Mg-G-acitn monomers were exposed to the synchrotron X-ray white beam for intervals of 0, 50, 100, and 200 ms and subjected to proteolysis using trypsin, Asp-N, and Glu-C. Comparison of the integrated peak areas for oxidized and unoxidized ions of peptides in the HPLC-ESI-MS chromatograms gives the extents of side-chain oxidation (Figure 1a), from which the loss of the unoxidized form can be fit to a first-order kinetics function (Figure 1b). The rate of oxidation for a particular peptide reflects the intrinsic reactivity of the side-chain

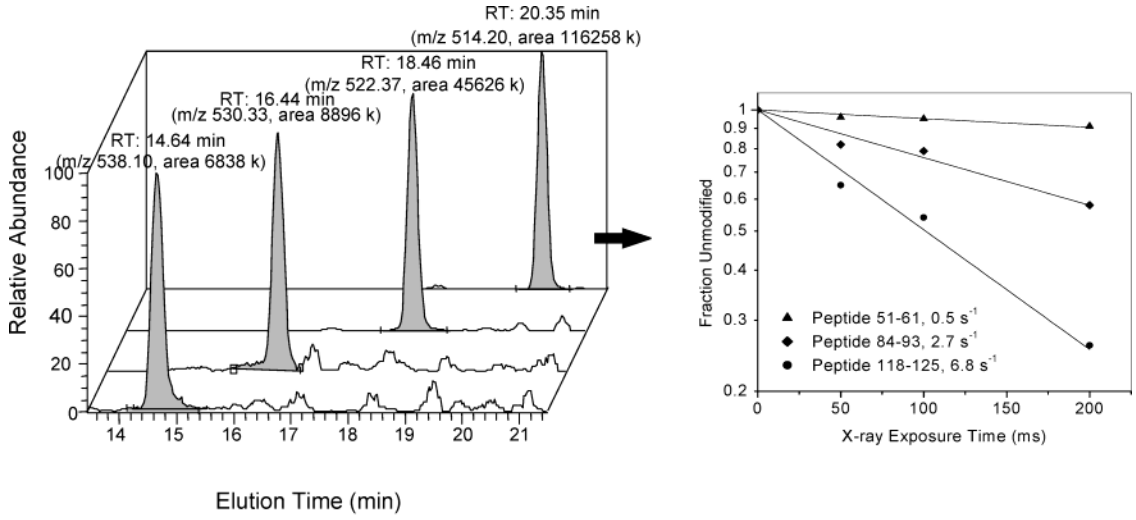

FIGURE 1: Quantification of modification extent for actin peptides. A representative chromatogram (a) is shown for unoxidized and oxidized peptides in HPLC/ESI-MS. Unoxidized (retention time, 20.35 min), singly oxidized (retention time 18.46 min), doubly oxidized (retention time, 16.44 min), and triply oxidized (retention time, 14.64 min) ions of peptide 118−125 of actin in the complex of Mg-G-actin/GS1 (exposure time 50 ms) were detected as doubly charged ions. Each plot with a given MS range was normalized to the largest peak in the specific range for the LC-run where the indicated peptide was located for the purposes of illustration. The extent of oxidation was calculated by using the TIC integrated areas (shown in the figure) of modified and unmodified species at each exposure time to give the dose response curves. (b) Dose response curves for peptides 51−61, 84−93, and 118−125 of actin in the Mg-G-actin/GS1 complex.

groups to hydroxyl radical attack, as well as its solvent accessibility. Figure 1b shows the different oxidation rates observed for three peptides, which reflect the unique combination of these two basic parameters for any individual peptide that is examined. MS/MS was used to identify the oxidized site(s) in a peptide as described previously (*23*, *24*, *26*, *27*, *29*). The oxidation rates and the oxidized residues for each peptide are summarized in Table 2. These results demonstrate an excellent correlation of side-chain reactivity with solvent accessibility for the actin crystal structures. For instance, the solvent accessible area values for the side chain of Tyr-53, which was identified by MS/MS to be the sole probe site in peptide 51−61, were seen in Table 1 to be 34 and 20 Å^2 for the Ca^{2+}-actin/GS1 and Mg^{2+}-actin/GS1 complexes, respectively, differing by a factor of 1.7 (Table 1), while the modification rates for peptide 51−61 for Ca^{2+}-G-actin/GS1 as compared to the Mg^{2+} form had a ratio of 1.9 (0.95 vs 0.5 s^{-1}, Table 2). For most side-chain residues, however, the solvent accessibilities in the two complexes are similar, as are the modification rates in the separate experiments. For example, the solvent accessible area for His-87, His-88, Phe-90, and Tyr-91, which were identified by MS/MS to be the oxidized sites in peptide 85−95, are 86, 25, 1, and 86 Å^2, respectively, in the complex of Ca^{2+}-actin/GS1. These surface area values remain almost unchanged in the complex of Mg^{2+}-actin/GS1: 90, 28, 0 and 81 Å^2. The measured oxidation rates for peptide 85−95 are 3.2 ± 0.5 and 3.0 ± 0.2 s^{-1} in the Ca^{2+}-G-actin/GS1 and Mg^{2+}-G-actin/GS1 complexes, respectively (i.e., identical within error). Note that the oxidation rate for peptide 85−95 is significantly higher than that of peptide 51−61, reflecting both the increased number of reactive groups and their increased relative accessibility in the former peptide.

Binding of gelsolin segment 1 to G-actin results in lower accessibility to the solvent of residues within the binding sites. This can be easily seen as a reduction in the rate of oxidation of peptide 337−339, for which the oxidation rates are 33 ± 3 and 29 ± 4 s^{-1} for the isolated Ca^{2+} and Mg^{2+} bound actin forms, respectively, while the oxidation rates for the corresponding GS1 bound monomers are 12 ± 2 and 14 ± 2 s^{-1}. Although this peptide has a complicated set of oxidizable residues, examination of the solvent accessibilities predicts a specific protection when the Ca^{2+}-actin/DNAse I structure is compared to either form of actin monomer bound to GS1 (Table 1). Overall, examination of the oxidation rates in Table 2 indicates similar rates of reaction for sites with similar structure and the relative rates correlate well with the number, type, and accessibility of the residues in the various peptides, consistent with previous structure/reactivity comparisons made with this technique (*22*−*28*). The data clearly indicate that the synchrotron footprinting method reliably reflects the solvent accessibility of a number of side-chain sites within the actin monomer—and connected with that—the expected differences in reactivity among the observed side chains.

Divalent Cation-Dependent Structure of Actin Monomers. Although crystallographic comparisons of Mg^{2+}- and Ca^{2+}-actin monomers bound to GS1 along with footprinting data in solution show little structural difference between the two forms, site-specific structural data on the comparable isolated actin monomers in solution have not been previously available. Analysis of the oxidation rate data for the 28 peptides derived from the trypsin, Asp-N, and Glu-C digestions reveal reactivity changes that are dependent on both divalent cation and GS1 binding. One peptide (51−61) shows Mg^{2+}-specific protections independent of GS1 binding. Eleven of the peptides show reduced oxidation rates for the isolated Mg^{2+}-G-actin monomer (11−23, 19−28, 40−50, 58−72, 63−68, 197−206, 196−207, 239−254, 242−253, 360−372, and 363−375) in comparison to the identical peptides in the isolated Ca^{2+}-G-actin (and compared to both actin/gelsolin segment-1 complexes). One peptide (337−359) exhibits a protection only for the GS1 bound form that is predicted from crystallographic data (see previously). Fifteen

Table 2: Modification Rate Data for Actin Peptides in Ca-G-Actin/GS1, Mg-G-Actin/GS1, Isolated Ca-G-Actin, and Isolated Mg-G-Actin[a]

peptide	protease	oxidized residues	subdomain	Ca-actin	Mg-actin	GS1-Ca-actin	GS1-Mg-actin	Ca-G-actin/ Mg-G-actin
1−18	trypsin	10C, 16L	1	7.3 ± 0.8	6.1 ± 0.5	6.8 ± 0.2	6.3 ± 0.6	1.2
19−28		21F	1	0.65 ± 0.07	0.32 ± 0.02	0.62 ± 0.02	0.57 ± 0.06	2.0[b]
40−50		40H, 44M, 47M	2	33 ± 6	20 ± 1	35 ± 5	40 ± 5	1.7[b]
51−61		53Y	2	0.69 ± 0.04	0.32 ± 0.01	0.95 ± 0.02	0.50 ± 0.02	2.1[b]
63−68		67L	2	0.40 ± 0.05	0.08 ± 0.02	0.46 ± 0.02	0.45 ± 0.04	5.0[b]
69−84		69Y,73H,79W,82M	1 + 2 (69)	7.3 ± 0.9	5.5 ± 0.7	7.3 ± 0.5	7.0 ± 0.4	1.3
85−95		87H, 88H, 90F, 91Y	1	2.8 ± 0.1	2.9 ± 0.1	3.2 ± 0.5	3.0 ± 0.2	1.0
96−113		101H,102P,110L,112P	1	0.50 ± 0.04	0.52 ± 0.04	0.65 ± 0.04	0.56 ± 0.04	1.0
119−147		119M,123M,124F,143Y	1+3 (143)	14 ± 2	12 ± 2	10 ± 2	13 ± 2	1.2
184−191		190M	4	10 ± 0.6	10 ± 2	12 ± 2	9.2 ± 1.1	1.0
197−206		200F-202 T[c]	4	0.83 ± 0.08	0.24 ± 0.01	0.75 ± 0.05	0.57 ± 0.06	3.4[b]
239−254		243P	4	0.75 ± 0.04	0.30 ± 0.02	1.2 ± 0.3	1.1 ± 0.2	2.5[b]
292−312		305M-307P	3	14 ± 2	11 ± 1	10 ± 2	11 ± 3	1.3
316−326		322 P, 325M	3	8.2 ± 0.4	6.1 ± 0.5	4.3 ± 0.9	7.3 ± 1.8	1.3
329−335		332P, 333P	3	0.78 ± 0.06	0.72 ± 0.03	0.69 ± 0.07	0.75 ± 0.03	1.1
337−359		337Y, 346L, 349L, 352F, 355M	link 1 + 3	33 ± 3	29 ± 4	12 ± 2	14 ± 2	1.1
360−372		362 Y, 367P, 371H	1	0.72 ± 0.03	0.38 ± 0.04	0.72 ± 0.03	0.74 ± 0.06	1.9[b]
11−23	AspN	21F	2	0.70 ± 0.04	0.43 ± 0.02	0.64 ± 0.07	0.53 ± 0.10	1.6[b]
157−178		161H, 164P, 166Y, 169Y, 171L-173L, 176M	3	9.8 ± 2.1	12 ± 2	6.1 ± 1.9	10 ± 3	0.8
222−243		227M,236L,243P	4	7.7 ± 1.0	6.5 ± 0.7	6.9 ± 1.2	7.0 ± 0.6	1.2
292−310		305M-307P	3	12 ± 2	12 ± 0.8	11 ± 2.4	12 ± 3	1.0
363−375		367P, 371H, 374C, 375F	1	8.5 ± 0.7	3.6 ± 0.05	6.1 ± 0.4	7.1 ± 0.5	2.4[b]
58−72	Gluc	67L, 69Y	2	1.1 ± 0.1	0.18 ± 0.04	1.1 ± 0.2	0.88 ± 0.15	6.1[b]
84−93		87H, 88H, 90F, 91Y	1	2.9 ± 0.2	2.8 ± 0.01	3.3 ± 0.4	2.7 ± 0.07	1.0
118−125		119M, 123M, 124F	1	8.4 ± 0.4	7.3 ± 1.0	8.9 ± 0.6	6.8 ± 1.0	1.1
196−207		200F-202 T[c]	4	1.1 ± 0.2	0.26 ± 0.02	0.82 ± 0.10	0.60 ± 0.13	4.2[b]
242−253		243P	4	0.69 ± 0.10	0.26 ± 0.01	0.90 ± 0.04	1.01 ± 0.21	2.6[b]
260−270		269M	4	7.9 ± 1.7	8.8 ± 1.1	11 ± 2	11 ± 3	0.9

[a] Column 1, residues of peptide; column 2, modified residues identified by MS/MS; column 3, subdomain location; columns 4−7, modification rate data for the four species (s^{-1}). For all samples, the actin concentration was kept at 5.0 μM and the $CaCl_2$ or $MgCl_2$ concentration was kept at 0.05 mM. The complexes were formed by mixing actin with GS1 in a molar ratio of 1:1.1 and were then incubated for 4−6 h before X-ray exposures. [b] The difference between the two actin forms is significant within error. [c] The specific probe site(s) cannot be determined definitively (see text).

Scheme 1

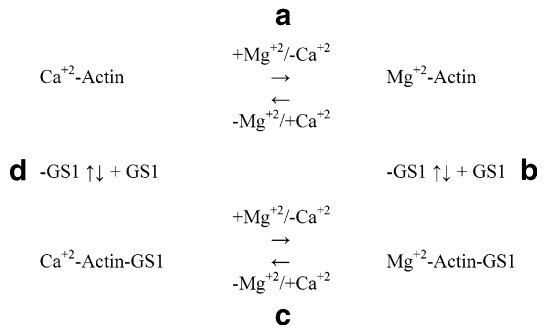

peptides (1−18, 69−84, 84−93, 85−95, 96−113, 118−125, 119−147, 184−191, 292−312, 157−178, 222−243, 260−270, 292−310, 316−326, and 329−335) show minimal or no differences in the oxidation rate for all four actin states, suggesting their reactivity is unchanged for the isolated monomers as compared to the monomers bound to GS1 irrespective of whether the sample contains Mg^{2+} or Ca^{2+}.

In Scheme 1, we outline the thermodynamic relationships among the four actin species studied in this work. Across the top (transition a) is indicated the reversible transition between the Ca^{2+} actin monomer and the Mg^{2+} actin monomer. As indicated previously, this transition is accompanied by specific changes in solvent accessibility for 11 separate peptides within the actin monomer, with the 19 sites (Table 2) becoming less accessible in the Mg^{2+} bound form relative to the Ca^{2+} bound form. Transition b indicates the reversible binding of GS1 to the Mg^{2+} actin monomer. The binding of GS1 results in a specific protection at the interface (peptide 337−359) and a loss of the protections seen in the formation of the Mg^{+2}-actin monomer in transition a. Most simply, GS1 binding to the Mg^{2+} monomer reverses the structural changes that were induced when Mg^{2+} replaced Ca^{2+}. Transition c, which involves the replacement of Mg^{2+} with Ca^{2+} as the divalent cation, is accompanied by no structural changes that can be detected by the footprinting method. However, transition d, the reversible binding of GS1 to the Ca^{2+} form, is accompanied by a change in the accessibility of side-chain residues within peptide 51−61, as well as the specific protection at the GS1 binding site seen in transition b.

Identification of Footprinting Probe Sites in G-Actin. The oxidation of most peptides results in oxidized species being shifted from the unmodified ion in most cases by unit oxygen masses (+16, +32, etc.), and MS/MS sequencing can be used to localize the specific sites of oxidation. A representative MS/MS spectrum is shown in Figure 2 for the singly oxidized and unoxidized form of peptide 184−191. In Figure 2a, in which the peptide did not receive any X-ray dose, *y*-ions (which are fragmentation products generated from the C-terminus) such as $y-3$, $y-4$, $y-5$, $y-6$, and $y-7$, and the *b*-ions (which are fragmentation products from the N-terminus) $b-4$, $b-5$, $b-6$, and $b-7$ can be identified. In contrast, for the oxidized peptide (Figure 2b), the *y*-ions are observed as $y2+16$, $y3+16$, $y4+16$, $y5+16$, and $y6+16$, implying that the oxidation occurred on Met-190 or Lys-191. The *b*-ion masses seen in the unmodified

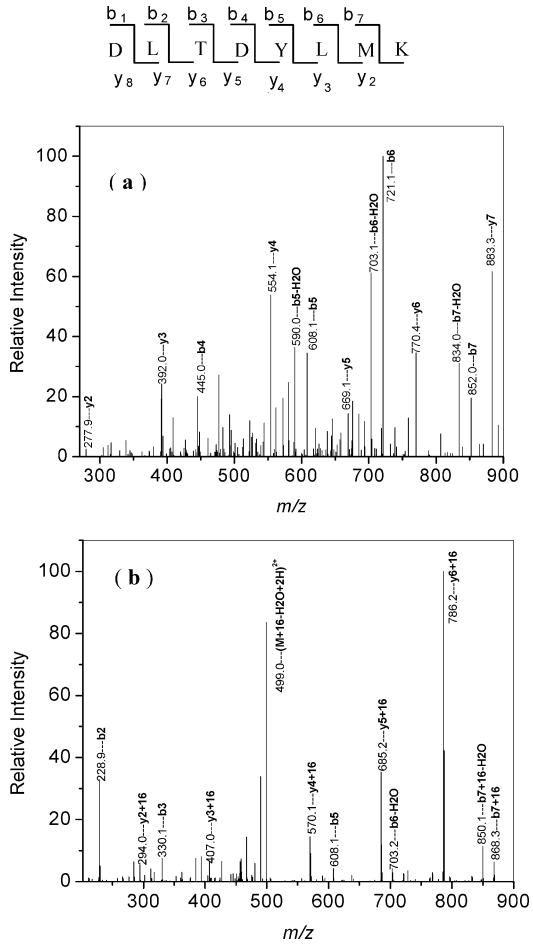

FIGURE 2: Representative MS/MS spectra are shown to identify the oxidation site for peptide 184−191. (a) MS/MS spectrum of unmodified peptide 184−191. (b) MS/MS spectrum for singly oxidized peptide 184−191.

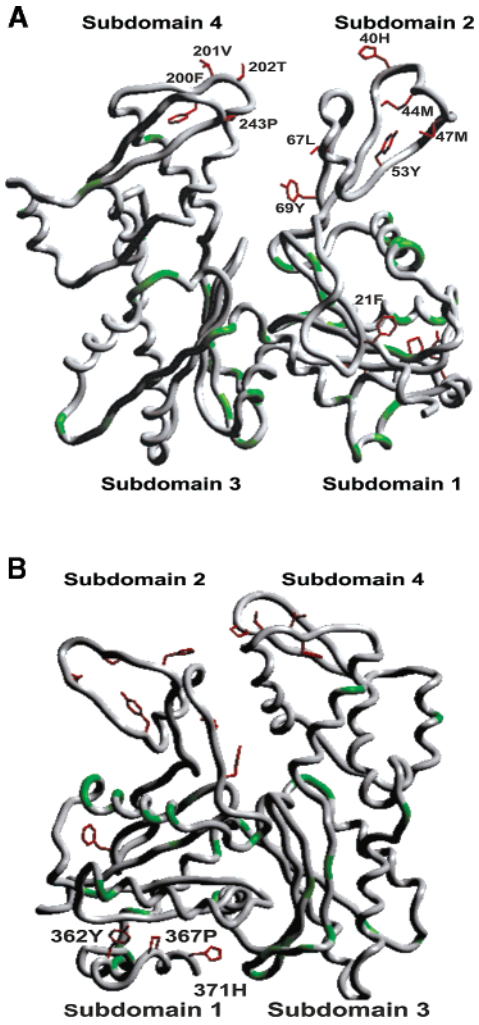

FIGURE 3: Actin monomer structure. The backbone trace shown in this figure is from the crystal structure of G-actin in the G-actin/DNase I complex with the DNase I removed (*12*). This actin structure does not have 374C and 375F since they were invisible in the electron density map collected in ref *12*. Colored in green are the backbones of the residues that are identified within peptides showing the same rate of reactivity for Ca-G-actin and Mg-G-actin. Colored in red are the sides chains of the residues from peptides that were observed to be less reactive in Mg-G-actin as compared to Ca-G-actin. (a) Probes that are involved in the conformational variation within subdomains 2 and 4. (b) Probes that are involved in the conformational variation within the C-terminus. Residues 374C and 375F at the very terminus were also monitored.

spectrum are still observed up to $b - 6$, however, the $b - 7$ ion was observed as +16 mass units, indicating that the oxidation occurred on Met-190. If oxidation occurs mainly on one residue of a peptide containing multiple modifiable residues, like peptide 184−191, the abundance of this modified residue will be far above those of the others that share the same *m*/*z*. However, if the oxidation sites are distributed among several modifiable residues in a peptide sequence, the tandem MS can identify all the residues contributing to the modification if the species ionizes and fragments well (e.g., sufficient signal-to-noise in the MS/MS spectrum is obtained). If the modification is distributed over several residues (such as for the case of peptide 197−206), and a good fragmentation pattern is not obtained, precisely locating the participating residues can be difficult.

The specific probe residues oxidized in each peptide were identified by MS/MS and are listed in Table 2, and some of the side chains are also illustrated in Figure 3 using the crystal structure of the G-actin DNase I complex (with DNase I removed for clarity). For isolated Ca^{2+} -G-actin, peptide 51−61 (with a probe residue of Tyr-53) shows an oxidation rate indistinguishable from that of its GS1 complex, while isolated Mg^{2+}-G-actin and its GS1 complex show 2−3-fold less reactivity at this site relative to the comparable Ca^{2+}-forms. Thus, Tyr-53 exhibits a Mg^{2+}-specific protection independent of GS1 binding.

Of the 11 peptides that exhibit a decrease in reactivity in isolated Mg^{2+}-actin, peptides 11−23, 19−28, 360−372, and 363−375 are located in subdomain 1; peptides 40−50, 58−72, and 63−68 are located in subdomain 2; and peptides 197−206, 196−207, 239−254, and 242−253 are located in subdomain 4 (Table 2). In subdomain 1, residues Tyr-362, Pro-367, His-371, Cys-374, and Phe-375 (from peptides 360−372 and 363−375) experience protection for isolated Mg^{2+}-actin (Figure 3). This Mg^{2+}-specific protection does not extend to the C-terminal GS1 binding site (341−355) or beyond, since peptide 337−359 experiences the same rate of oxidation for both the isolated Ca^{2+}- and Mg^{2+}-G-actin forms as also does peptide 329−335. Phe-21 in subdomain 1, which is observed in two separate peptides (11−23 and 19−28), also experiences a protection in isolated Mg^{2+}-G-actin.

Oligomerization States of Ca^{2+}- and Mg^{2+}-G-Actin. Oligomerization of Mg-G-actin monomers is well-documented (*35*−*37*); however, oligomerization in footprinting experiments would seriously complicate any interpretation of protections. Our results show clearly that numerous sites in Mg^{2+}-G-actin monomers experience a widespread range of protections relative to the Ca^{2+} monomer forms. To confirm that these protections are specifically induced by the conformational variations of isolated G-actins, dynamic light scattering (DLS) was used to test the homogeneity of Ca^{2+}-G-actin and Mg^{2+}-G-actin under solution conditions identical to those used in the footprinting experiments. The total intensity of scattered light is sensitive to both the concentration and the particle size, particularly the latter (*38*, *39*), and DLS experiments can report changes in both these parameters and provide a shape-dependent calculated hydrodynamic radius (*40*, *41*). We found that when the actin concentration was varied from 3 to 10 μM, the scattered light intensity measured at an angle of 90° rose moderately for Ca^{2+}-G-actin and Mg^{2+}-G-actin samples at divalent cation concentrations of 0.2 or 0.05 mM (data not shown), indicative of an increase only in the monomer concentration. The calculated hydrodynamic radius of the observed species in these experiments was ∼2.2 nm. As the actin concentration is increased above 10 μM, a steeply cooperative increase in hydrodynamic radius and in scattered light intensity is observed for the isolated Mg^{2+} samples as a function of actin concentration, while the Ca^{2+}-G-actin solutions exhibit no changes in the hydrodynamic radius up to actin concentrations of 30 μM. This is consistent with the known differences in divalent ion dependence of oligomerization (*35*−*37*). Since all protein footprinting experiments were carried out at an actin monomer concentration of 5 μM, the footprinting results are interpreted in terms of changes in monomer structure and dynamics.

DISCUSSION

Mg^{2+}-Dependent Protections of G-Actin in the D-Loop and at the C-Terminus. As most of the peptides monitored for Ca-G-actin outside the GS1 contact interface behave similarly with those in the actin/GS1 complexes, the structure of Ca-G-actin in solution is judged to be similar to the actin structure within the GS1 complexes. In sharp contrast to the corresponding residues in Ca-G-actin, residues 40H, 44M, 47M, 53Y, 67L, and 69Y in subdomain 2, residues 200F-202T and 243P in subdomain 4, and residues in the C-terminal region (in subdomain 1) had reduced reactivity (the reductions ranged from 40 to 80%) in Mg-G-actin. Some of the protected residues above are located on structural elements that contribute to intermolecular contacts in the model of F-actin structure (Table 3, see later) (*34*). This work suggests that structural changes at these sites occur already at the stage of a Ca^{2+} to Mg^{2+} switch in the actin monomer. Also, the data show that this Mg^{2+}-dependent conformational change is reversed upon GS1 binding. A consistent structural explanation for many of these changes would be the possible existence of a narrower cleft between subdomains 2 and 4 in Mg-G-actin (Figure 3). Many of the protected side-chain residues illustrated in Figure 3 are directed inward toward the cleft, making this explanation quite plausible. The protections at 200F-202T and 243P, which could be the result of the tip of subdomain 4 making closer contact with subdomain 2 (or vice-versa), are also consistent with the model of F-actin and are the first evidence for conformational variations in these loops, which may be relevant to actin polymerization. In fact, a recent study has shown that a yeast actin double mutant with alterations in subdomain 2 at positions 204 (A204E) and 243 (P243K) does not polymerize (*42*).

Table 3: Protection Sites Predicted in the Holmes Model and in This Footprinting Work[a]

residue probes at the contact sites predicted by Holmes model	subdomain	protection in Mg-G-actin vs Ca-G-actin?
322	3	×
243	4	○
202	4	○
166	3	×
169	3	×
375	1	○
44	2	○
47	2	○
110	1	×
112	1	×
269	4	×

[a] 11 probe sites predicted to contribute to contacts between actin monomers within the context of the actin filament model (*34*). At five of these sites, we observe protections in Mg-G-actin (○, including 44M, 47M, 202T, 243P, and 375F). Six of these residues (×, including 110L, 112P, 166Y, 169Y, 269M, and 322P) do not exhibit similar structural rearrangements in our study.

In the atomic structure of Ca-G-actin (in the actin/DNase I complex), loop 69−78 together with residues 33−35 constitutes a hinge linking subdomains 1 and 2. The protection of 67L and 69Y observed in this work also suggests alterations in the conformation of this region in Mg-G-actin. These conformational variations are consistent with changes in proteolytic susceptibility in this region, specifically, a Mg^{2+}-dependent inhibition of trypsin cleavage at Arg 62 and Lys68 has been observed (*43*). The protection observed for 40H, 44M, and 47M shows that the DNase-binding loop is less solvent accessible in the Mg-G-actin form.

Flexibility of the DNase-binding loop has been observed in a number of crystal structures for complexed G-actins. While in the complex of G-actin/DNase I the DNase-binding loop (38−52) (*12*) was seen to be folded as a β-turn, it is disordered in the complexes of G-actin/GS1 (*13*, *17*). In the crystal structure of TMR-blocked ADP-G-actin, the DNase-binding loop (observed as His-40∼Gly-48) is folded as an α-helix (*18*), and as compared to that of G-actin in the ATP-G-actin/DNase complex, the orientations of subdomains 2 and 4 are rotated by ∼10 and ∼5°, respectively. Our footprinting results highlight the divalent cation-dependent conformational variations that can be induced in this loop.

The proposed Mg-dependent structural alternations in the subdomain 2 region for Mg-G-actin extend to some residues in subdomain 1 that are close to subdomain 2, such as 21F monitored in peptides 11−23 and 19−28 (Table 2). Consistent with this finding is the report that the binding of specific antibodies to residues 18−29 is observed only for Ca-G-actin, not for Mg-G-actin (*3*, *44*). However, the structural alterations observed above do not extend all the way to the N-terminus, as residues Cys-10 and Leu-16 appear to have the same solvent accessibility for both Ca- and Mg-

G-actins (Table 2). This is also consistent with binding data; antibodies specific to residues 1−7 bind equally well to Ca- and Mg-G-actins (*3*). Therefore, it appears that residues 1−16 at the N-terminus have similar solvent accessibility for both Ca- and Mg-G-actins. A Mg-dependent protection for G-actin was not observed for peptide 119−147 (Table 2); this peptide has several possible probes including 119M, 123M, 124Y, and 143Y, and the reactivity of this peptide is dominated by the reactivity from the two methionine residues. Thus, although this peptide covers α-helix 137−144, which was predicted to mediate narrowing of the cleft between subdomain 2 and 4 (*45*), it is not likely to be sensitive to local structural reorganizations.

Unlike the residues in the N-terminus, the residues in the C-terminus were protected in Mg-G-actin, as monitored by peptide 360−372 from the trypsin digestion and peptide 363−375 from the AspN digestion. These protections suggest that the C-terminus in Mg-G-actin may be closer to the core of subdomain 1 than in Ca-G-actin. The more tightly packed conformation of the C-terminus in Mg-G-actin may be responsible for the enhanced fluorescence of fluorophores coupled to Cys-374, as observed by Frieden and colleagues (*46*, *47*). Conformational alteration at the C-terminus has also been observed through a fluorescent label attached to Lys-373 (*48*) and in an EPR study showing an increased rigidity of the environment of Cys-374 in Mg-G-actin as compared to Ca-G-actin (*8*). The observation that trypsin cleavage at Arg-372 and Lys-373 in Mg-G-actin proceeds 4−6 times more slowly than in Ca-G-actin is also entirely consistent with our footprinting results (*43*).

The compaction of subdomain 1 and the closer approach between subdomains 2 and 4 as observed above raises the question as to the structural basis of this conformational change. High-resolution crystallographic data on GS1-actin complexes in both the Mg^{2+}-ATP and the Ca^{2+}-ATP bound forms indicate significant differences in the metal-coordination environment that are likely linked to the conformational changes observed in this study (*13*, *17*). Mg^{2+} is six-coordinate, while Ca^{2+} can have coordination numbers from 6 to 9 (a coordination number of 7 is seen for Ca^{2+}-ATP bound actin forms). In addition, although both metal ions strongly prefer oxygen ligands, the average metal−ligand distances for Mg^{2+}-coordination complexes are typically shorter by 0.3−0.4 Å (*54*). The shorter bond lengths for Mg^{2+} and a smaller coordination number may result in structural changes in the network of coordinated water molecules that drive divalent cation-dependent conformational changes. However, since their changes are reversed by GS1 binding, the relationship between the metal ion-coordination environment and footprinting sensitive structural changes is far from simple.

Divalent Cation Independent Structural Features of G-Actin. Many residues monitored in subdomains 1, 3, and 4 do not show appreciable differences in reactivity between Ca- and Mg-G-actins. These residues include the linker between subdomain 1 and 3 (monitored as peptide 337−359) and the putative hydrophobic loop (monitored as peptide 260−270) that has been assumed to form a hydrophobic plug in actin filaments (*34*), as well as many other segments (such as helices 84−93, 118−125, 316−326, and 222−243). Molecular dynamics simulations (*49*) suggested that narrowing the cleft between subdomains 2 and 4 of Mg-ATP-G-actin would be accompanied by a detachment of the 262−274 loop from the surface of subdomain 4. Our study provides no support for this change under the experimental conditions of this paper, although this loop does appear to detach when filaments are formed (*50*, *51*). However, these results suggest that Ca^{2+}-G-actin and Mg^{2+}-G-actin share similar conformations within many regions of subdomains 1, 3, and 4.

Allosteric Communication between Actin Subdomains. It has been proposed that there is an intramolecular coupling among the structures of the DNase-binding loop, the C-terminus, and the hydrophobic plug in the formation of actin filaments (*19*, *20*, *52*, *53*). Although we do not observe changes in the hydrophobic loop, potential allosteric communication between subdomain 2 and the C-terminus is implicated by this study. This suggests that the Mg-G-actin may more closely resemble the structure of the subunits in actin filaments and that the observed structural features could act as an activator for polymerization, which may to some degree explain the lower critical concentration for polymerization, higher polymerization rate, lower depolymerization rate, and higher nucleation rate observed for Mg-G-actin as compared to Ca-G-actin (*5*).

Table 3 shows 11 probe sites predicted to contribute to contacts between actin monomers within the context of the actin filament model (*34*). At five of these sites, we observe protections in Mg-G-actin (including 44M, 47M, 202T, 243P, and 375F). This may indicate that the Mg^{2+}-dependent structural rearrangements at these sites facilitate filament assembly. Six of these residues (110L, 112P, 166Y, 169Y, 269M, and 322P) do not exhibit similar structural rearrangements in our study. Nevertheless, further conformational alterations of Mg-G-actin may continue to occur during the course of actin filament formation, including the proposed changes in the putative hydrophobic loop and the linker between subdomains 1 and 3.

Four additional sites monitored in this footprinting work (residues 53Y, 67L, 69Y, and 371H) are not predicted to be at the contact interface in F-actin but do exhibit Mg^{2+}-dependent protections. Three of these residues are within subdomain 2 adjacent to its cleft with subdomain 4 (Figure 3a), and one residue is in the interface between subdomains 1 and 3 (Figure 3b). We examined the potential ability of these sites to participate in protein−protein interactions by reanalyzing the surface accessibility calculations while using a large probe radius (>5 Å). The use of a larger probe radius reduced the solvent accessibility of these residues to effectively zero, indicating that it is unlikely they can participate in protein−protein interactions (the opposite results were seen for those residues predicted to be involved in filament interactions above). The role of these residues may be related to mediating allosteric conformational changes necessary for filament assembly.

Consistent with previous crystallographic investigations of G-actin complexes and with observations of local conformational differences between Ca- and Mg-G-actin using fluorescent probes and antibodies, the present study provides detailed, global structural information for isolated G-actins in solution, illustrating divalent cation-dependent conformational variations in G-actin. The use of footprinting techniques extends crystallographic and other spectroscopic studies by providing data on structural reorganizations at the

level of specific amino acids or their clusters, without the potential risk of site perturbation by the attached probes. This approach can be applied to many complexes of monomeric and filamentous actin as well as to other protein systems.

SUPPORTING INFORMATION AVAILABLE

Two figures. This material is available free of charge via the Internet at http://pubs.acs.org.

REFERENCES

1. Pollard, T. D., Blanchoin, L., and Mullins, R. D. (2000) *Annu. Rev. Biophys. Biomol. Struct. 29*, 545−576.
2. Higgs, H. N., and Pollard, T. D. (2001) *Annu. Rev. Biochem. 70*, 649−676.
3. Mejean, C., Hue, H. K., Pons, F., Roustan, C., and Benyamin, Y. (1988) *Biochem. Biophys. Res. Commun. 152*, 368−375.
4. Orlova, A., and Egelman, E. H. (1993) *J. Mol. Biol. 232*, 334−341.
5. Estes, J. E., Selden, L. A., Kinosian, H. J., and Gershman, L. C. (1992) *J. Muscle Res. Cell Motil. 13*, 272−284.
6. Slosarek, G., Heintz, D., and Kalbitzer, H. S. (1994) *FEBS Lett. 351*, 405−410.
7. Strzelecka-Golaszewska, H., Wozniak, A., Hult, T., and Lindberg, U. (1996) *Biochem. J. 316*, 713−721.
8. Nyitrai, M., Hild, G., Belagyi, J., and Somogyi, B. (1997) *Biophys. J. 73*, 2023−2032.
9. Nyitrai, M., Hild, G., Lakos, Z., and Somogyi, B. (1998) *Biophys. J. 74*, 2474−2481.
10. Moraczewska, J., Wawro, B., Seguro, K., and Strzelecka-Golaszewska, H. (1999) *Biophys. J. 77*, 373−385.
11. Blanchoin, L., and Pollard, T. D. (2002) *Biochemistry 41*, 597−602.
12. Kabsch, W., Mannherz, H. G., Suck, D., Pai, E. F., and Holmes, K. C. (1990) *Nature 347*, 37−44.
13. McLaughlin, P. J., Gooch, J. T., Mannherz, H.-G., and Weeds, A. G. (1993) *Nature 364*, 685−692.
14. Schutt, C. E., Myslik, J. C., Rozycki, M. D., Goonesekere, N. C. W., and Lindberg, U. (1993) *Nature 365*, 810−816.
15. Head, J. F., Swamy, N., and Ray, R. (2002) *Biochemistry 41*, 9015−9020.
16. Otterbein, L. R., Cosio, C., Graceffa, P., and Dominguez, R. (2002) *Proc. Natl. Acad. Sci. U.S.A. 99*, 8003−8008.
17. Vorobiev, S., Strokopytov, S., Drubin, D. G., Frieden, C., Ono, S., Condeelis, J., Rubenstein, P. A., and Almo, S. C. (2003) *Proc. Natl. Acad. Sci. U.S.A. 100*, 5760−5765.
18. Otterbein, L. R., Craceffa, P., and Dominguez, R. (2001) *Science 293*, 708−711.
19. Kim, E., and Reisler, E. (1996) *Biophys. J. 71*, 1914−1919.
20. Kim, E., and Reisler, E. (2000) *Biophys. Chem. 86*, 191−201.
21. Kim, E., Wriggers, W., Phillips, M., Kokabi, K., Rubenstein, P. A., and Reisler, E. (2000) *J. Mol. Biol. 299*, 421−429.
22. Chance, M. R. (2001) *Biochem. Biophys. Res. Commun. 287*, 614−621.
23. Goldsmith, S. C., Guan, J.-Q., Almo, S. C., and Chance, M. R. (2001) *J. Biomol. Struct. Dyn. 19*, 405−418.
24. Guan, J.-Q., Vorobiev, S., Almo, S. C., and Chance, M. R. (2002) *Biochemistry 41*, 5765−5775.
25. Guan, J.-Q., and Chance, M. R. (2003) *Encycl. Mol. Biol.*, in press.
26. Kiselar, J. G., Maleknia, S., Sullivan, M., Downard, K., and Chance, M. R. (2002) *Int. J. Rad. Biol. 78*, 101−114.
27. Kiselar, J. G., Janmey, P., Almo, S. C., and Chance, M. R. (2003) *Proc. Natl. Acad. Sci. U.S.A. 100*, 3942−3947.
28. Rashidzadeh, H., Khrapunov, S., Chance, M. R., and Brenowitz, M. D. (2003) *Biochemistry 42*, 3655−3665.
29. Maleknia, S. D., Brenowitz, M., and Chance, M. R. (1999) *Anal. Chem. 71*, 3965−3973.
30. Spudich, J. A., and Watt, S. (1971) *J. Biol. Chem. 246*, 4866−4871.
31. Yao, X., Grade, S., Wriggers, W., and Rubenstein, P. A. (1999) *J. Biol. Chem. 274*, 37443−37449.
32. Nyman, T., Schuler, H., Korenbaum, E., Schutt, C. E., Karlsson, R., and Lindberg, U. (2002) *J. Mol. Biol. 317*, 577−589.
33. Yao, X., Nguyen, V., Wriggers, W., and Rubenstein, P. A. (2002) *J. Biol. Chem. 277*, 22875−22882.
34. Holmes, K. C., Popp, D., Gebhard, W., and Kabsch, W. (1990) *Nature 347*, 44−49.
35. Mozo-Villarias, A., and Ware, B. R. (1985) *Biochemistry 24*, 1544−1548.
36. Newman, J., Estes, J. E., Selden, L. A., and Gershman, L. C. (1985) *Biochemistry 24*, 1538−1544.
37. Attri, A. K., Lewis, M. S., and Korn, E. D.(1991) *J. Biol. Chem. 266*, 6815−6824.
38. Arosio, D., Kwansa, H. E., Gering, H., Piszczek, G., and Bucci, E. (2002) *Biopolymers 63*, 1−11.
39. Ferre-D'Amare, A., and Burley, S. (1997) *Methods Enzymol. 276*, 157−166.
40. Bell, C. E., Poon, P. H., Schumaker, V. N., and Eisenberg, D. (1997) *Biochemistry 36*, 15201−15207.
41. MacColl, R., Malak, H., Crycznski, I., Eisele, L. E., Mizejewski, G. J., Franklin, E., Sheikh, H., Montellese, D., and MacColl, L. C. (1998) *Biochemistry 37*, 417−423.
42. Trybus, K. M., personal communication.
43. Strzelecka-Golaszewska, H., Moraczewska, J., Khaitlina, S. Y., and Mossakowska, M. (1993) *Eur. J. Biochem. 211*, 731−742.
44. Adams, S. B., and Reisler, E. (1994) *Biochemistry 33*, 14426−14433.
45. Tirion, M. M., and ben-Avraham, D. (1993) *J. Mol. Biol. 230*, 186−195.
46. Frieden, C., Lieberman, D., and Gilbert, H. R. (1980) *J. Biol. Chem. 255*, 8991−8993.
47. Frieden, C. (1982) *J. Biol. Chem. 257*, 2882−2886.
48. Carlier, M.-G., Pantaloni, D., and Korn, E. D. (1986) *J. Biol. Chem. 26*, 10785−10792.
49. Wriggers, W., and Schulten, K. (1997) *Biophys. J. 73*, 624−639.
50. Shvetsov, A., Musib, R., Phillips, M., Rubenstein, P. A., and Reisler, E. (2002) *Biochemistry 41*, 10787−10793.
51. Guan, J.-Q., and Chance, M. R., unpublished results.
52. Orlova, A., and Egelman, E. H. (1995) *J. Mol. Biol. 245*, 582−597.
53. Feng, L., Kim, E., Lee, W. L., Miller, C. J., Kuang, B., Reisler, E., and Rubenstein, P. A. (1997) *J. Biol. Chem. 272*, 16829−16837.
54. Bertini, I., Gray, H. B., Lippard, S., and Valentine, J. (1994) *Bioinorganic Chemistry*, p 110, University Science Books, Mill Valley, CA.

BI034914K